

UC Berkeley

UC Berkeley Previously Published Works

Title

Untethered subcentimeter flying robots.

Permalink

<https://escholarship.org/uc/item/7bv7w59s>

Journal

Science Advances, 11(13)

Authors

Sui, Fanping

Yue, Wei

Behrouzi, Kamyar

et al.

Publication Date

2025-03-28

DOI

10.1126/sciadv.ads6858

Peer reviewed

ENGINEERING

Untethered subcentimeter flying robots

Fanping Sui^{1,2†}, Wei Yue^{1,2†}, Kamyar Behrouzi^{1,2}, Yuan Gao^{1,2}, Mark Mueller², Liwei Lin^{1,2*}

The miniaturization of insect-scale flying robots with untethered flights is extremely challenging as the tradeoff between mass and power becomes problematic. Here, a subcentimeter rotating-wing robot of 21 mg in weight and 9.4 mm in wingspan driven by a single-axis alternating magnetic field has accomplished navigable flights. This artificial flying robot is the lightest and smallest to realize untethered and controllable aerial travels including hovering, collision recovery, and route adjustments. Experimentally, it has achieved a high aerodynamic efficacy with a measured lift-to-drag ratio of 0.7 and lift-to-flying power ratio of 7.2×10^{-2} N/W at a Reynolds number of ~2500. The wireless driving mechanism, system operation principle, and flight characteristics can be further optimized for the advancement and miniaturization of subcentimeter scale flying robots.

INTRODUCTION

The miniaturization of flying robots has been explored over the past decades with considerable efforts (1–11) to tackle key fundamental challenges such as the powering strategy, propulsion efficiency, and aerodynamics. As the system mass/wingspan decreases, electrical wires have been used to deliver power instead of using onboard batteries or supercapacitors for payload reductions (7–11). However, these tethered flying robots have struggled to operate freely in complex environments. Recent breakthroughs in centimeter-scale flying robots have used external energy sources—such as light, wind, and electromagnetic wave—for successful untethered flights (1, 2, 4–6). On the other hand, the usages of magnetic field and actuation mechanism are also attractive to wirelessly power robots with good controllability and rapid responses. These include a flat bar with multimodal locomotion (12), helical-shape micro-swimmers (13–16), nanowire-based motors (17, 18), and self-assembled beads (19, 20). Specifically, these magnetic robots have high working mobility except possible interferences of high-permeability materials for either surface or underwater locomotion without the capability to fly. Here, we show a 9.4-mm untethered flying robot powered by a single-axis alternative magnetic field to achieve controllable flights, such as hovering, collision survival, and route adjustment.

Apart from the power source, another major challenge in the field of miniaturized flying robots is the stability of the flight attitude, which is closely linked to maneuverability. In principle, a robot can fly if its driving mechanism provides sufficiently high lift force to overcome gravity. In practice, attitude stability is equally important for stable and controllable flights. For instance, several previously reported aerial robots do not have good attitude stability such that they can only take off and fly under the help of fixed supporting structures (21–24). Although active negative feedback control has been used to maintain the attitude stability in large-scale flying robots via complex onboard/external sensing and control systems (9, 10, 25), these setups require heavy payloads that are not feasible for subcentimeter scale flying robots.

Here, an untethered flying robot driven by a single-axis alternating magnetic field is proposed to simultaneously address the issues

of power, attitude stability, and maneuverability. Figure 1A shows the schematic view of the subcentimeter flying robot in an alternating magnetic field, and Fig. 1B shows a fabricated prototype, where a pair of permanent magnets (gray color) is fixed to the main body (white color) consisting of the propeller blade and balance ring. The magnetic orientation of the magnets attempts to align with the direction of the external magnetic field for minimum magnetic energy by the magnetic torque τ

$$\tau = \mathbf{m} \times \mathbf{B} \quad (1)$$

where \mathbf{m} and \mathbf{B} represent the magnetic moment vector of the magnets and the external magnetic field vector, respectively. This torque induces the continuous rotation of the propeller in the alternating magnetic field to generate the lift force. The balance ring enhances the attitude stability and maneuverability by increasing the rotational inertia of the flying robot for a sizable angular momentum along the rotational axis under high-frequency spinning conditions. This results in a strong gyroscopic effect to improve the stability of the flight attitude.

RESULTS

Robot design and operation principle

The prototype robot comprises two key components: (i) a main body structure of four propeller blades and a balance ring fabricated by three-dimensional (3D) printing process (14.7 mg) and (ii) two tiny permanent magnets fixed on the main body. Each magnet has a mass of 3.15 mg, a diameter of 1 mm, and a thickness of 0.5 mm. The total weight of the prototype robot is 21 mg, and the wingspan is 9.4 mm—the smallest among published works to achieve untethered and maneuverable aerial flights. The blade geometry is determined through a trial-and-error experimental modification process for operations in low Reynold number regions, including aerodynamic performance factors such as stability and efficiency. This design process can be scaled to different sizes (figs. S1 and S2) with the scaling analysis in the Supplementary Materials. Figure 1C (movie S1) shows the sequential frames of an upward flight for a total traveling distance of ~4 cm in 138 ms under an alternating magnetic field of 21 mT at 340 Hz. It is observed that the robot maintains its upright posture (flight attitude) throughout the whole flight with good stability.

The uniaxial alternating magnetic field, \mathbf{B} , is analyzed by drawing a circle as shown in the inset in Fig. 2A using the amplitude of the alternating magnetic field, B_0 , as the radius, with a circulating

Copyright © 2025 The Authors, some rights reserved; exclusive licensee American Association for the Advancement of Science. No claim to original U.S. Government Works. Distributed under a Creative Commons Attribution NonCommercial License 4.0 (CC BY-NC).

¹Berkeley Sensor and Actuator Center, University of California at Berkeley, Berkeley, CA 94720, USA. ²Mechanical Engineering Department, University of California at Berkeley, Berkeley, CA 94720, USA.

*Corresponding author. Email: lwlin@berkeley.edu

†These authors contributed equally to this work.

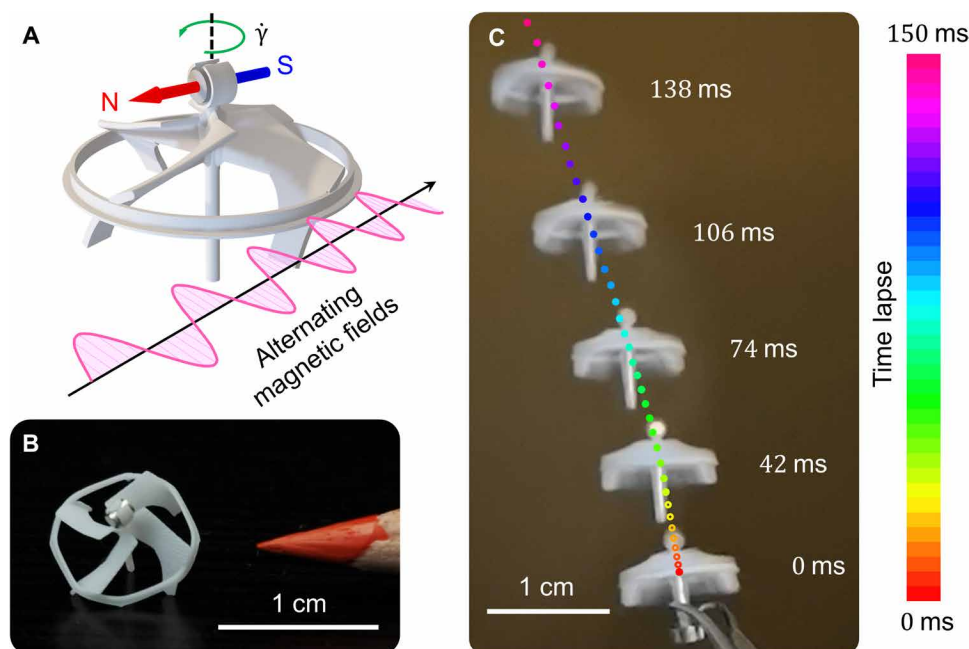


Fig. 1. Working principle of the untethered subcentimeter scale flying robot. (A) Schematic diagram of the powering scheme by the single-axis magnetic field. (B) Optical image of a 21-mg prototype alongside a pencil with a wingspan of 9.4 mm. (C) Sustained rotational motions and takeoff of the robot with the stable attitude (maintaining the vertical posture throughout the flight) and increased vertical velocity in time-lapse optical images. The solid dots represent experimental results, while the circles represent interpolated results.

frequency, ω_{ext} (the frequency of the alternating magnetic field). Hence, the x -directional component at any point of the circle matches the strength of the alternating magnetic field with an equivalent rotational angle, $\arcsin(B/B_0)$. Magnets with the remanence vector, \mathbf{M}_{rem} , on the robot are actuated by this external magnetic field with a rotational angle, γ . Under the appropriate magnetic field strength and frequency, the magnetic north of the robot can rotate with an angular velocity, $\dot{\gamma}$, to follow the external magnetic field with a lagging angle, $\Delta\Phi$, approximated as (see the Supplementary Materials)

$$\Delta\Phi \approx \arcsin \frac{2M_D}{V_{\text{mag}} M_{\text{rem}} B_0} \quad (2)$$

where M_D is the drag torque, which is a function of the frequency of the alternating magnetic field; V_{mag} is the total volume of the magnets; and M_{rem} is the remanence of the magnets. Analytically, as the alternating magnetic field reaches its maximum value at point (I) with the leftward direction, the magnetic north makes the counterclockwise rotational motion behind it due to the lagging magnetic torque with an angle of $\sim 12^\circ$ in this drawing. At point (II), the magnetic north reaches the leftward direction at 90° , and the time delay between points (I) and (II) can be calculated as $\Delta\Phi / \omega_{\text{ext}}$. The magnetic field strength reaches its maximum at point (I) and decreases continuously until it reaches zero at point (III). In this process, the rotational inertia effect of the robot helps its continuous counterclockwise rotation while its angular velocity decreases slightly due to the reduction of the magnetic torque. Point (IV) shows that the magnetic north reaches the downward direction at 180° , and the time delay between points (III) and (IV) can also be calculated as $\Delta\Phi / \omega_{\text{ext}}$.

Experimentally, an optical setup has been used to measure the lagging angle by a high-speed camera (fig. S4). The angular velocity

is calculated via a video tracking algorithm and an imaging processing technique with respect to the corresponding time in one cycle (fig. S5). Measurements (dots for individual and solid lines for average values) and simulations (dashed lines) in one cycle are recorded as shown in Fig. 2 (A and B), including the external magnetic flux density (pink), $\sin\gamma$ (green), and the angular velocity of the flying robot (blue) with respect to time under a driving frequency of 320 Hz for the 9.4-mm robot in an alternating magnetic field of 16.1 mT. The rotational motion responds to the alternating magnetic field with a lagging angle, $\Delta\Phi$ (12° in this case), which results in the fluctuation of the induced angular velocity (more experimental results for other conditions in fig. S6). By using the cubic spline regression scheme, the experimentally measured data between angular velocity and time is approximated as a curve (dark blue) shown in Fig. 2B. The prototype robot has a nonuniform angular velocity as expected as the result of the driving mechanism by a single-axis alternating magnetic field. Nevertheless, under a relatively high operating frequency, the angular velocity is relatively uniform with small variations of less than 10%.

The influences of the magnetic field strength and driving frequency with respect to the lagging angle $\Delta\Phi$ under the condition that the robot can rotate continuously are shown in Fig. 2C from both experiments (circular symbols) and simulations (color map). Analytically, the air-drag torque depends on the angular velocity (driving frequency) and the magnetic torque is proportional to the product of $\sin\Delta\Phi$ and the magnitude of the magnetic field. In these analyses, the lagging angle is a crucial parameter for sustained stable flights as the air-drag torque and magnetic torque should be approximately equal to reduce the fluctuations of the angular velocity. For example, the increase in the magnetic field amplitude can result in the reduction of the lagging angle for a constant magnetic torque under the same driving frequency and vice versa.

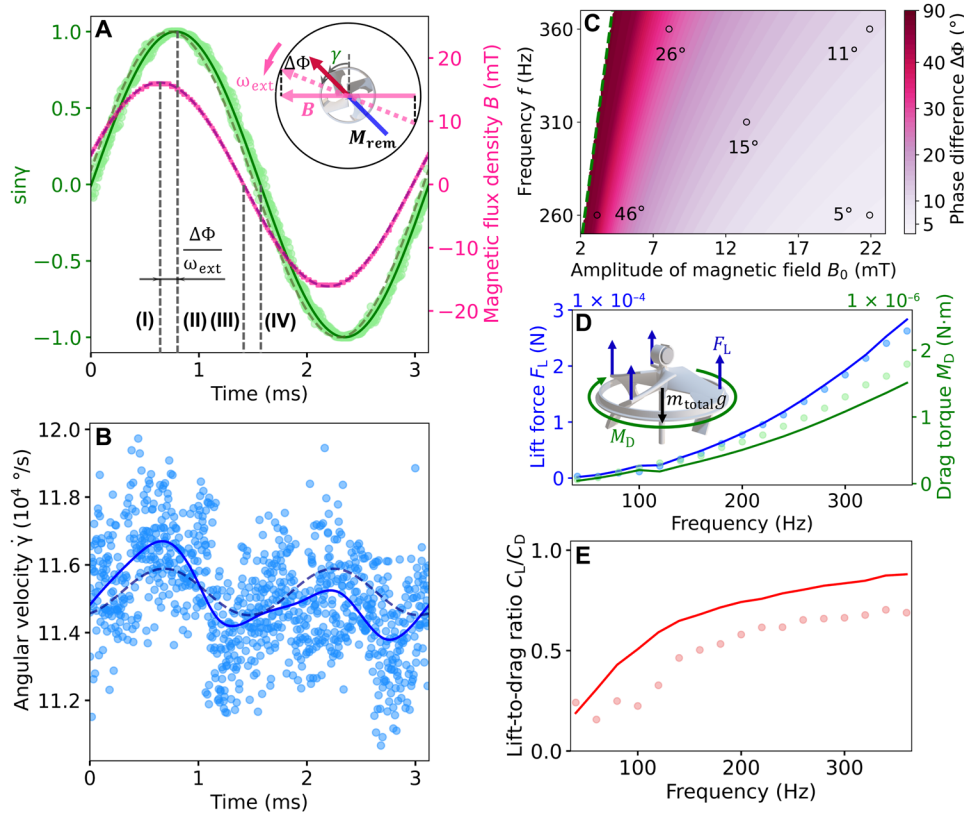


Fig. 2. Rotational kinematics and aerodynamic performance. Measurement results for the 9.4-mm robot in an alternating magnetic field of 16.1 mT in amplitude under a driving frequency of 320 Hz (dots for individual values and solid lines for average values) and simulation results (dashed lines): (A) the external magnetic flux density (pink), $\sin \gamma$ (green) with respect to time, and (B) the angular velocity of the flying robot (blue) with respect to time. The rotational motion of the robot responds to the alternating magnetic field with a lagging angle, $\Delta \Phi$ (12° in this case), which results in the fluctuation of the induced angular velocity. (I), (II), (III), and (IV) in (A) correspond to the time when the magnetic field reaches its maximum, the magnetic north points leftward, the magnetic field drops to zero, and the magnetic north points downward, respectively. (C) Experimental (dots) and analytical (color map) results of lagging angles for the flying robot with respect to the driving frequency and the amplitude of the alternating magnetic field. The color map represents analytical results that correspond well with experimental results. The green dashed line under low magnetic fields represents the operating conditions under low magnetic power supplies, and the robot fails to rotate continuously above this line due to the high air-drag torque. Measured (dots) and predicted (lines) results of: (D) lift force (blue), drag torque (green), and (E) lift-to-drag ratio (red) versus the driving frequency.

In experimental tests, the robot is found to automatically adjust its lagging angle to accommodate the magnetic field strength variations under a specific driving frequency, which simplifies the flight operation to maintain stability. The lagging angle of 90° is a critical point, where the flying robot fully uses the external magnetic field to balance the drag torque and it also defines the lowest magnetic field strength to balance the drag torque for sustained flight at a given frequency. For the 9.4 mm prototype robot, the minimum takeoff frequency is 310 Hz and the lowest magnetic field magnitude to maintain the flight is 3.1 mT.

A simplified aerodynamic model is established with ANSYS Fluent (version 2021) to study the underlying airflow patterns and provide design guidelines for the flying robots. In this model, a robot is put inside a rotating cylinder to analyze the rotational effect, and the system is placed inside a large cylinder to capture the induced air flow in the surrounding environment (fig. S7). The aerodynamic characteristics are studied for both the air flow velocity and pressure fields surrounding the robot at different driving frequencies. The negative and positive pressure distributions on the top and bottom surfaces of the blade result in the net lift force, F_L and drag torque, M_D (fig. S8)

$$F_L = \mathbf{e}_3 \cdot \iint_{S_0} \mathbf{n} \cdot \tilde{\mathbf{P}}(x, y, z) dS \quad (3)$$

$$M_D = \mathbf{e}_3 \cdot \iint_{S_0} \mathbf{r}(x, y, z) \times [\mathbf{n} \cdot \tilde{\mathbf{P}}(x, y, z)] dS \quad (4)$$

where $\mathbf{r}(x, y, z)$ represents the location vector from the center of the robot, dS represents the infinitesimal surface area as the variable of integral, \mathbf{n} represents the unit vector with the normal direction of the surface area, \mathbf{e}_3 represents the unit vector along the symmetry axis, S_0 represents the entire surface of the flying robot, and $\tilde{\mathbf{P}}(x, y, z)$ represents the pressure tensor. Specifically, the vertical experimental speed of 0.4 m/s under a driving frequency of 350 Hz is used in simulations. Experimentally, the lift force, F_L , is characterized by using a custom-made force measurement system, and the drag torque, M_D , is characterized by capturing the angular acceleration, $\dot{\gamma}$, from the recorded video when the magnetic field is turned off (fig. S9). Results in Fig. 2D show that both the measured lift force (blue dots) and drag torque (green dots) increase as the driving frequency increases, which corresponds well with simulation results (blue and green lines, respectively). The deviation of the air-drag torque between experiment and simulation mainly comes from the nonzero frictional losses of the supporting bearing system, which is used in experiments but not in simulations. The lift-to-drag ratio curve is

derived by the radius of the wing, R_r , as $C_L / C_D = R_r F_L / M_D$, where C_L is the lift coefficient and C_D is the drag coefficient in Fig. 2E. It is observed that the lift-to-drag ratio increases monotonically with respect to the driving frequency until around 250 Hz, where the ratio approaches 0.7. After that, it reaches an approximate plateau phase where the ratio increases slowly due to two factors. First, at a low driving frequency, the viscous drag effect dominates in the low Reynolds number regime, while this effect generally reduces as the Reynolds number increases. Second, at a high driving frequency, the pressure drag gradually increases to be larger than that of the viscous drag such that the lift-to-drag ratio mainly depends on the pressure distributions (26) to gradually reach a plateau phase.

The takeoff operation starts by placing the robot on a bearing system using a holder (tweezer) with the upright orientation under a low alternating magnetic field strength (~3.4 mT) with a low driving frequency (~40 Hz). Next, a low airflow (such as 0.01 m/s in magnitude) by a hair dryer is applied to induce a counterclockwise rotational motion for a positive lift force. The airflow is turned off as the driving frequency increases gradually. In this process, the circuit for the magnetic field (fig. S3) is progressively switched toward low capacitance modes to increase the resonant frequency of the inductor-capacitor network and to increase the maximum magnetic field strength. After the speed of the propeller increases to a designated operation frequency range (310 to 350 Hz), the robot generates high enough lift force to take off from the holding bearing. The takeoff driving frequency is determined by aerodynamic simulations and experiments to balance the trade-offs between the lift-to-drag ratio, power, and the operational complexity. First, the driving frequency should be sufficiently high in the lift-to-drag ratio plot (Fig. 2E) to efficiently use the magnetic power. Second, the driving frequency cannot be too high for avoiding the high air-drag torque. To be more specific, the lift-to-flying power ratio (LFPR) is defined as the lift force divided by the energy consumed in the flying robot. A high driving frequency could result in a low LFPR value for a low system efficiency to generate the lift force. Third, a very high operation frequency requires multiple switching steps, which increases the operation complexity. Specifically, a frequency window between 310 and 350 Hz for the 9.4-mm prototype is obtained by numerical simulations and experiments under a magnetic field strength of 16.1 mT. The minimum takeoff frequency is found at 310 Hz for the hovering flight, while the robot flies and accelerates upward under a higher driving frequency of 340 Hz as shown in movie S1.

The attitude and lateral flight movement of the flying robot are highly coupled. As the robot tilts from the upright posture, the lateral component of the lift force induces lateral movements. Therefore, it is critical to maintain the flight attitude for the robot to keep its lateral position. Furthermore, external disturbances such as airflows and possible collisions with small or large objects will disrupt the motion states. Most flying robots use integrated and/or external sensors/control systems to manage disturbances (9, 10), and flight stability is often achieved by positioning the center of pressure above the center of mass for the whole system. This provides passive stability by creating negative feedback to maintain an upright posture and mitigate unwanted lateral movements (3, 27). However, this also introduces an increased payload burden due to the possible additional mass. Here, the mass distribution is optimized by using a balance ring to enhance stability via the gyroscopic effect, while the increased moment of inertia along the axis of symmetry helps resist disturbances and reduce flight attitude changes.

Upward, hovering, and collision flights

The upward flights (~10 tests) are demonstrated with good attitude stability as shown in Fig. 3A by maintaining the upright posture, and the deviation from the vertical angle is also recorded. The camera used in this work has its own internal algorithm by turning on the high-speed mode after some initial delays such that points with dashed lines are used for regions without the high-speed mode. It is found that the robot takes off for a sustained flight with a duration of 143 ms in this case, with an average vertical acceleration of 1.4 m/s^2 . Figure 3B shows the corresponding flying height and pitch angle with respect to time. The pitch angle shows a periodically varied pattern with a frequency of around 30 Hz with the root mean square deviation and maximum peak-to-peak value of 1.1° and 5.2° , respectively. In this experiment, the lift force generated by the flying robot exceeds its own weight by approximately 14%, and this value can be increased further by using a high driving frequency to carry extra payloads. For example, a 110-mg passive sensing system is integrated onto the balance ring of a 20.5-mm flying robot (mass: 162.4 mg, operating frequency: 180 Hz, as in fig. S1) to detect the environmental infrared radiation intensity. The flying robot successfully takes off and measures the infrared intensity distribution during the upward flight with results shown in fig. S10 and movie S8.

The short-term hovering flight is defined as maintaining the flight position for a certain amount of time, and video recordings are qualitative validations. The quantitative validations evaluate the flying position and attitude with respect to time. In general, the recorded duration of all hovering flights (~10) is less than 0.5 s as the flying robot often accidentally collides with the experimental setup to markedly change the flight status and move out of the camera view. Figure 3C shows a 422-ms hovering flight of a 9.4-mm prototype with a driving frequency of 300 Hz, which is slightly below the takeoff frequency of 310 Hz to maintain the hovering state (movie S2). In this case, the lift force is slightly lower than the gravity such that the robot moves downward before it hits the wall at 241 ms. It then moves leftward quickly due to the collision impact and maintains its attitude until it hits the experimental setup at 400 ms. During this process, the flying robot survives the first collision without falling to the ground, while the impact changes the upward velocity from -83 to 67 mm/s and horizontal velocity from 190 to -426 mm/s as shown in Fig. 3D. The pitch angle variation is less than 5° throughout the collision process for good stability.

Furthermore, the flight attitude of the flying robot can change notably after a collision and recover afterward via the self-stabilization process as shown in Fig. 3E. In this case, the 9.4-mm prototype collides with the experimental setup after 27 ms (movie S3) to result in a large pitch angle fluctuation of 14.6° in Fig. 3F. The undesirable pitch angle fluctuation gradually reduces to 3.6° at 232 ms after the impact for the robot to recover back to its initial attitude. It is noted that the recovery after collisions is a probabilistic event depending on the magnitude, angle, surface, and other factors of the impact. A total of 34 collision flight tests for the 9.4-mm robot are conducted, and the robot survives in 26 tests without falling to the ground immediately for a survival rate of 76.5%. Furthermore, it is observed that the flight is recoverable after the impact if the pitch angle deviation is less than $\sim 23^\circ$ after a collision (movie S4). A 26.7-mm flying robot (mass: 220.2 mg, operating frequency: 122 Hz, as in fig. S1) is tested for impulsive disturbances by releasing isopropyl alcohol droplets $\sim 1 \text{ cm}$ above the robot (fig. S11 and movie S5). In experiments, the robot is allowed to hover in space with two thin strings connected

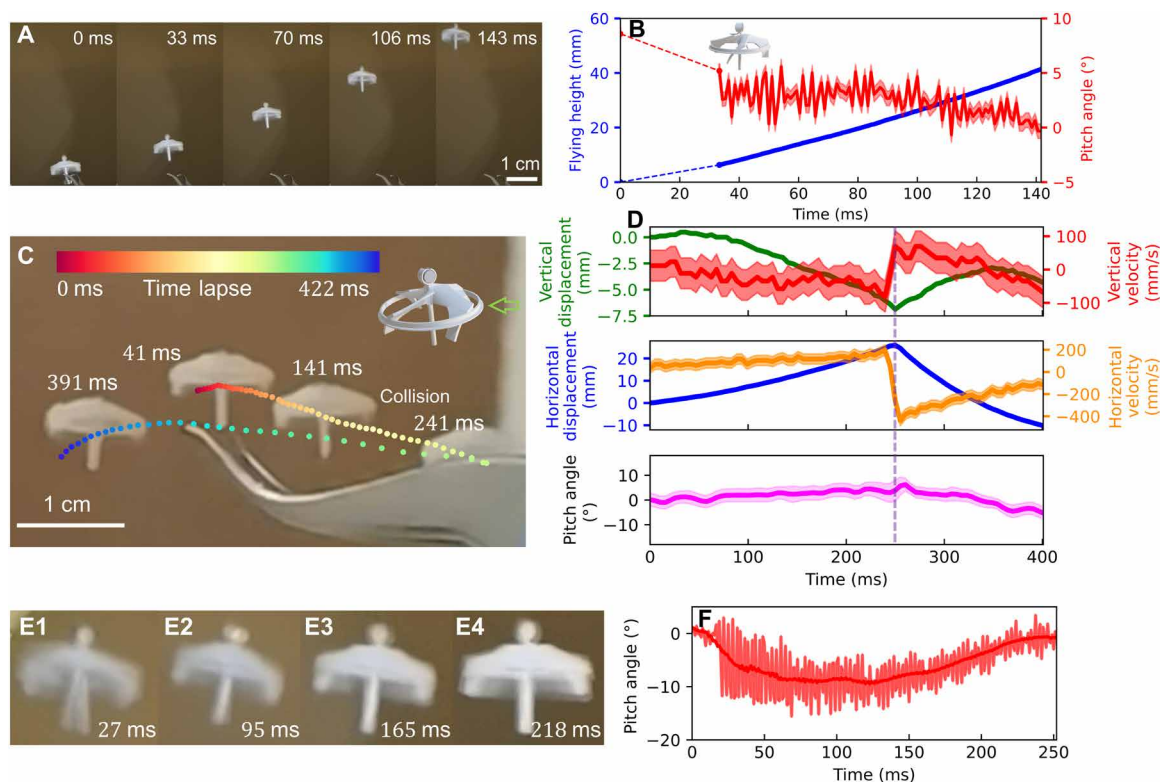


Fig. 3. Untethered flight demonstrations of upward, hovering, collision survival, and attitude recovery. (A) Optical images for the sustained upward flights. (B) Corresponding flying heights and pitch angles with respect to time. Points with dashed lines at the beginning of the flying represent the data from the low-speed camera. (C) Optical images showing the hovering and collision stability test. Initially, the robot moves rightward and collides with the side wall after 241 ms. It then moves leftward due to the impact as indicated in the inset figure and maintains its attitude stability. (D) Corresponding vertical, horizontal displacement, and velocity measurements with respect to time and the pitch angle measurement with respect to time. The light purple dashed line represents the time when the collision takes place. The shaded area represents measurement errors. (E) Optical images and (F) pitch angle changes illustrating an attitude recovery process for a 9.4-mm prototype after a collision. The robot gradually recovers back to its initial attitude after the collision. The black arrow represents the time when the collision takes place. The darker red line represents the averaged pitch angle.

to a bearing system fixed on the ground. It is observed that when the flying robot is in a state of high-frequency rotation, the change of the pitch angle due to the droplet is minimal to demonstrate the flight stability with the help of the gyroscopic effect.

Vertical robot movements are strongly affected by the driving frequency, while their lateral motions can be regulated by the gradient of the applied magnetic field. In general, regions with high magnetic flux densities are energetically favorable for the robot to reduce the total potential energy, and this can be used to guide the lateral movements of the robot. The gradient-induced lateral force, F_T , is characterized experimentally by a custom-made force measurement system (fig. S12). It is found that the lateral force depends linearly on the magnetic field gradient, ∇B_0 , near the takeoff frequency (fig. S13A). In addition, experiments show that the variation of the lateral force divided by the variation of the magnetic field gradient is independent of the frequency both near and above the takeoff frequency (fig. S13B). These characteristics provide valuable control guidelines and strategies to maneuver untethered flights for various flight patterns and paths. For example, left or right turn can be obtained by an open-loop control scheme with appropriate driving frequency, magnetic field distribution, initial position, and initial attitude. The trajectory adjustments such as turns are accomplished by modulating the spatial distribution of the magnetic field gradient using a single

coil setup. For example, a controlled left-turn flight is accomplished by the 9.4-mm prototype in Fig. 4A with the magnetic field intensity distribution (max value of 22 mT) in Fig. 4B (movie S6). The 9.4-mm prototype under a driving frequency of 320 Hz takes off with an initial pitch angle of 2° (measured in the experiment) at the position 20 mm below and 2 mm left to the center of the magnetic coil. It flies both upward and leftward with distances of 23.5 and 24.3 mm, respectively, after 191 ms. Both the horizontal (Fig. 4C) and vertical (Fig. 4D) motions are related to the corresponding components of the magnetic field gradient-induced force, respectively. As the robot experiences a horizontal magnetic gradient field with an increasing magnitude from -0.02 T/m at 0 ms to -0.3 T/m at 191 ms, the measured horizontal acceleration changes from -1.8 m/s² at the beginning to -4.5 m/s² at the end of the flight. It is also noted that a downward magnetic gradient field also exists with a maximum value of 0.2 T/m from 0 to 66 ms, and a vertical acceleration of -1.3 m/s² is measured. After 66 ms, the robot reaches the region where the vertical component of the corresponding magnetic field is relatively uniform, such that the vertical acceleration gradually increases to 0 and becomes positive. Experimental results also show that the torque induced by the magnetic field density gradient can result in the increment of the pitch angle from its original upright position to a specific tilt angle as the robot is observed to tilt counterclockwise with

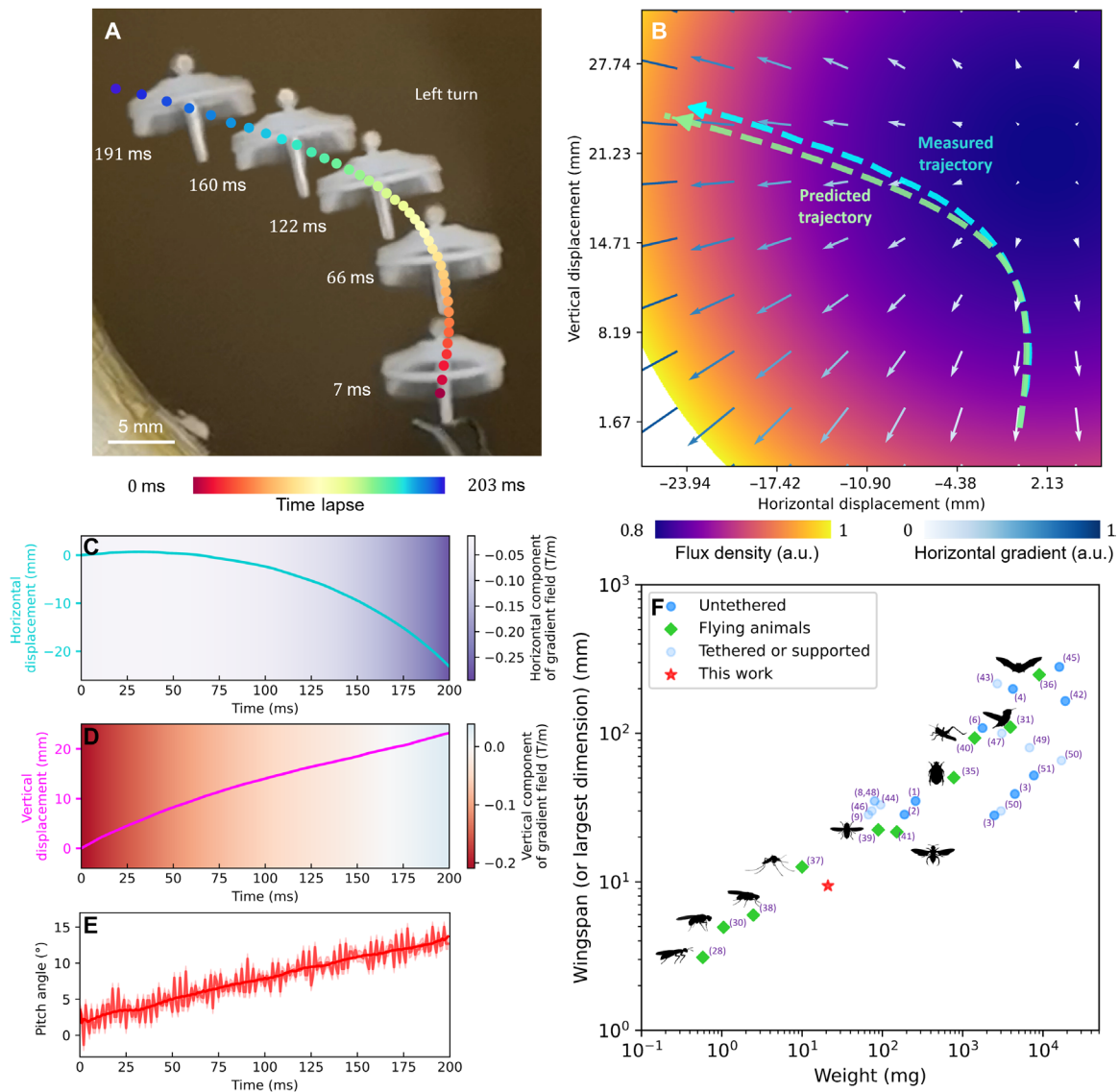


Fig. 4. Left-turn flight and comparison with state of the art. (A) Time-lapse optical image of a left-turn flight for the 9.4-mm prototype by using the magnetic field gradient effect. (B) Corresponding magnetic flux density color map and magnetic field gradient distributions with flight trajectories. The blue-white arrows represent the magnetic field gradient distribution (the directions, lengths, and colors of the arrows for the directions, magnitudes, and horizontal components of the magnetic field gradient, respectively). The light blue and light green dashed lines represent measured and predicted flight trajectories, respectively. (C and D) Corresponding measured displacements and the magnitude of the magnetic field gradient along the horizontal and vertical direction with respect to time. (E) Experimental pitch angle with respect to time. (F) Wingspan (or the largest dimension) versus the weight of living animals (green), untethered flying robots (dark blue), tethered or supported flying robots (light blue), and this work (red). a.u., arbitrary unit.

a pitch angle of 16° at 191 ms as shown in Fig. 4E. At 205 ms, the robot has a moderate collision with the side surface of the magnetic coil and moves backward and disappears in the screen. A dynamic model is developed on the basis of the dynamics of rigid bodies (see the Supplementary Materials and fig. S14). The experimental results of the flight trajectory at 320 Hz match well with the numerical modeling results among different driving frequencies as shown in fig. S15. As expected, a high driving frequency results in a low turning curvature, while a low driving frequency results in a high turning curvature. The controlled right-turn flight is also realized as shown in fig. S16 (movie S7) to illustrate the repeatability of the proposed

maneuvering methodology by showing that similar initial conditions can result in the flying robot to follow a nearly identical trajectory.

Comparison with state of the art

The key progresses in miniaturized flying robots are illustrated in the characteristic dimension versus weight plot in Fig. 4F for different flying objects, including living animals (28–41) and untethered and tethered robots with and without successful flight demonstrations (1, 3, 4, 6, 7, 10, 11, 42–51). Previously, the smallest reported flying robot (either tethered or untethered) with successful aerial flights is 28 mm in diameter (3), while natural flying insects can be

as small as 0.15 mm (52), which serves as a key inspiration for the continuing miniaturization of flying robots. It is noted that untethered flying robots generally have heavier weights compared to those of living animals of similar wingspan dimensions. This implies that artificial flying robots are constrained by their construction materials and functional components, which results in inferior flight efficiencies and heavier weights as compared to those of flying insects. For example, on-board energy resources can notably increase the weight of artificial robots. Hence, when the mass of the robot is reduced to less than 1 g, there are only three successful untethered flying robots, including the 256-mg Robobee X-wing (1), 190-mg laser-powered aerial vehicle (2), and the 21-mg prototype robot in this work. They all use external energy sources instead of on-board energy storage devices for weight reductions. In this figure, the smallest flying object is a female *Nasonia vitripennis* with a wingspan of only 3 mm and a weight of 0.58 mg. More details are in table S1.

An important aerodynamic attribute is the LFPR, which has been characterized and compared with other works and living animals (1, 3, 4, 6, 7, 10, 11, 28–34, 42, 43, 45–49) as shown in fig. S17. The converted external energy used by the flying robot (including those of tethered robots) is used as the input energy for the calculation instead of the total energy for the whole experimental setup. The prototype in this work successfully demonstrates controlled and untethered flight, with a measured input power level of less than 3.0 mW for hovering operation and an LFPR of 0.072 N/W, which surpasses most other studies and is only slightly lower than that of the 4.21-g CoulombFly and the 16-g DelFly II. The high LFPR achieved in this work is the result of remote energy supply without on-board energy sources and efficient aerodynamics designs (details in table S2).

DISCUSSION

By regulating a single-axis alternating magnetic field, a class of untethered insect-scale flying robots with high aerodynamic efficiency and inherent stability has been realized with various flight maneuvering demonstrations. Analytical models, numerical simulations, and experimental results are thoroughly studied with good consistency to illustrate the importance of key design features and provide critical guidelines for possible further miniaturizations. The structural approach for stable operations and the magnetic field gradient for the flight path controls help the subcentimeter scale flying robot to exhibit untethered flights such as hovering, turning, and collision recovery without complex sensing or controlling electronics. While these achievements advance the field of insect-scale flying robots, the future grand challenge remains to emulate or even exceed the capabilities of real flying insects. Some possible future directions and challenges include: (i) the utilization of advanced multicoil systems (53–55) and further miniaturization of the robot to achieve wider flying ranges (see the Supplementary Materials); (ii) new design, material, and mechanism to improve the flight control and increase the payload capacity; (iii) on-board energy conversion devices to convert magnetic energy to electricity to power additional electrical components; and (iv) wireless communication systems with low latency wireless link for information exchanges. These and other efforts could eventually lead to the performance improvement of insect-scale flying robots to emulate subcentimeter flying insects for practical and important tasks in applications such as performing gastrointestinal endoscopy and in-pipe inspection in limited and confined spaces or conducting search and rescue, environmental monitoring, and agricultural supports in open areas.

MATERIALS AND METHODS

Fabrication of the flying robot

The main body is constructed using the Form 3 printer (Formlabs Inc.), with an X-Y resolution of 25 μm and a horizontal layer thickness of 50 to 100 μm , using White V4 or Clear V4 materials. Two N52-grade NdFeB permanent magnets (1 mm in diameter and 0.5 mm in length) from TRYMAG Inc. are fitted into two notches on the robot, with the notches having a diameter 10% larger than that of the magnet. The magnets attract each other to complete the assembly process.

Lift force and lateral force measurement systems

The measurement system comprises a 3D printed lever, two 681ZZ metal shield ball bearings at the fixed hinge, and a force sensor. The levers are 3D printed by Markforged X7 (Markforged Inc.) with a resolution of 50 μm by using carbon fibers. The force sensor with a resolution of 0.01 mN is disassembled from a commercial analytical balance (Bonvoisin Inc.) and used in this work.

Supplementary Materials

The PDF file includes:

Supplementary Text
Figs. S1 to S17
Tables S1 and S2
Legends for movies S1 to S8
References

Other Supplementary Material for this manuscript includes the following:

Movies S1 to S8

REFERENCES AND NOTES

- N. T. Jafferis, E. F. Helbling, M. Karpelson, R. J. Wood, Untethered flight of an insect-sized flapping-wing microscale aerial vehicle. *Nature* **570**, 491–495 (2019).
- J. James, V. Iyer, Y. Chukewad, S. Gollakota, S. B. Fuller, Liftoff of a 190 mg laser-powered aerial vehicle: The lightest wireless robot to fly, in *IEEE International Conference on Robotics and Automation (ICRA)* (IEEE, 2018), pp. 3587–3594.
- M. Piccoli, M. Yim. Piccolissimo: The smallest micro aerial vehicle, in *IEEE International Conference on Robotics and Automation (ICRA)* (IEEE, 2017), pp. 3328–3333.
- W. Shen, J. Peng, R. Ma, J. Wu, J. Li, Z. Liu, J. Leng, X. Yan, M. Qi, Sunlight-powered sustained flight of an ultralight micro aerial vehicle. *Nature* **631**, 537–543 (2024).
- B. H. Kim, K. Li, J.-T. Kim, Y. Park, H. Jang, X. Wang, Z. Xie, S. M. Won, H.-J. Yoon, G. Lee, W. J. Jang, K. H. Lee, T. S. Chung, Y. H. Jung, S. Y. Heo, Y. Lee, J. Kim, T. Cai, Y. Kim, P. Prasopsukh, Y. Yu, X. Yu, R. Avila, H. Luan, H. Song, F. Zhu, Y. Zhao, L. Chen, S. H. Han, J. Kim, S. J. Oh, H. Lee, C. H. Lee, Y. Huang, L. P. Chamorro, Y. Zhang, J. A. Rogers, Three-dimensional electronic microfilers inspired by wind-dispersed seeds. *Nature* **597**, 503–510 (2021).
- T. Ozaki, N. Ohta, T. Jimbo, K. Hamaguchi, A wireless radiofrequency-powered insect-scale flapping-wing aerial vehicle. *Nat. Electron.* **4**, 845–852 (2021).
- K. Y. Ma, P. Chirattananon, R. J. Wood, Design and fabrication of an insect-scale flying robot for control autonomy, in *IEEE/RSJ International Conference on Intelligent Robots and Systems (IROS)* (IEEE, 2015), pp. 1558–1564.
- R. J. Wood, The first takeoff of a biologically inspired at-scale robotic insect. *IEEE Trans. Robot.* **24**, 341–347 (2008).
- S. B. Fuller, M. Karpelson, A. Censi, K. Y. Ma, R. J. Wood, Controlling free flight of a robotic fly using an onboard vision sensor inspired by insect ocelli. *J. R. Soc. Interface* **11**, 20140281 (2014).
- K. Y. Ma, P. Chirattananon, S. B. Fuller, R. J. Wood, Controlled flight of a biologically inspired, insect-scale robot. *Science* **340**, 603–607 (2013).
- D. S. Drew, N. O. Lambert, C. B. Schindler, K. S. J. Pister, Toward controlled flight of the Ionocraft: A flying microrobot using electrohydrodynamic thrust with onboard sensing and no moving parts. *IEEE Robot. Autom. Lett.* **3**, 2807–2813 (2018).
- W. Hu, G. Z. Lum, M. Mastrangeli, M. Sitti, Small-scale soft-bodied robot with multimodal locomotion. *Nature* **554**, 81–85 (2018).
- L. Zhang, J. J. Abbott, L. Dong, B. E. Kratochvil, D. Bell, B. J. Nelson, Artificial bacterial flagella: Fabrication and magnetic control. *Appl. Phys. Lett.* **94**, 064107 (2009).
- X. Z. Chen, J.-H. Liu, M. Dong, L. Müller, G. Chatzipirpiridis, C. Hu, A. Terzopoulou, H. Torlakcik, X. Wang, F. Mushtaq, J. Puigmartí Luis, Q. D. Shen, B. J. Nelson, S. Pané,

- Magnetically driven piezoelectric soft microswimmers for neuron-like cell delivery and neuronal differentiation. *Mater. Horiz.* **6**, 1512–1516 (2019).
15. S. Tottori, L. Zhang, F. Qiu, K. K. Krawczyk, A. Franco-Obrégón, B. J. Nelson, Magnetic helical micromachines: Fabrication, controlled swimming, and cargo transport. *Adv. Mater.* **24**, 811–816 (2012).
 16. A. Ghosh, P. Fischer, Controlled propulsion of artificial magnetic nanostructured propellers. *Nano Lett.* **9**, 2243–2245 (2009).
 17. W. Gao, S. Sattayasamitsathit, K. M. Manesh, D. Weihs, J. Wang, Magnetically powered flexible metal nanowire motors. *J. Am. Chem. Soc.* **132**, 14403–14405 (2010).
 18. L. Zhang, T. Petit, Y. Lu, B. E. Kratochvil, K. E. Peyer, R. Pei, J. Lou, B. J. Nelson, Controlled propulsion and cargo transport of rotating nickel nanowires near a patterned solid surface. *ACS Nano* **4**, 6228–6234 (2010).
 19. I. Petousis, E. Homburg, R. Derks, A. Dietzel, Transient behaviour of magnetic micro-bead chains rotating in a fluid by external fields. *Lab Chip* **7**, 1746–1751 (2007).
 20. C. E. Sing, L. Schmid, M. F. Schneider, T. Franke, A. Alexander-Katza, Controlled surface-induced flows from the motion of self-assembled colloidal walkers. *Proc. Natl. Acad. Sci. U.S.A.* **107**, 535–540 (2010).
 21. P. Bhushan, C. Tomlin, Design of an electromagnetic actuator for an insect-scale spinning-wing robot. *IEEE Robot. Autom. Lett.* **5**, 4188–4193 (2020).
 22. Z. Liu, X. Yan, M. Qi, D. Huang, X. Zhang, L. Lin, Electrostatic flapping-wing actuator with improved lift force by the pivot-spar bracket design. *Sens. Actuators A Phys.* **280**, 295–302 (2018).
 23. X. Yan, M. Qi, L. Lin, Self-lifting artificial insect wings via electrostatic flapping actuators, in *IEEE 28th International Conference on Micro Electro Mechanical Systems (MEMS)* (IEEE, 2015), pp. 22–25.
 24. Z. Liu, X. Yan, M. Qi, X. Zhang, L. Lin, Low-voltage electromagnetic actuators for flapping-wing micro aerial vehicles. *Sens. Actuators A Phys.* **265**, 1–9 (2017).
 25. P. Chirarattananon, K. Y. Ma, R. J. Wood, Adaptive control of a millimeter-scale flapping-wing robot. *Bioinspir. Biomim.* **9**, 025004 (2014).
 26. A. Kourta, A. Thacker, R. Joussot, Analysis and characterization of ramp flow separation. *Exp. Fluids.* **56**, 104 (2015).
 27. M. Piccoli, M. Yim, Passive stability of a single actuator micro aerial vehicle, in *IEEE International Conference on Robotics & Automation (ICRA)* (IEEE, 2014), pp. 5510–5515.
 28. F.-O. Lehmann, N. Heymann, Dynamics of in vivo power output and efficiency of *Nasonia* asynchronous flight muscle. *J. Biotechnol.* **124**, 93–107 (2006).
 29. R. K. Josephson, R. D. Stevenson, The efficiency of a flight muscle from the locust *Schistocerca americana*. *J. Physiol.* **442**, 413–429 (1991).
 30. F. O. Lehmann, M. H. Dickinson, The changes in power requirements and muscle efficiency during elevated force production in the fruit fly *Drosophila melanogaster*. *J. Exp. Biol.* **200**, 1133–1143 (1997).
 31. D. J. Wells, Muscle performance in hovering hummingbirds. *J. Exp. Biol.* **178**, 39–57 (1993).
 32. M. H. Dickinson, J. R. B. Lighton, Muscle efficiency and elastic storage in the flight motor of *Drosophila*. *Science* **268**, 87–90 (1995).
 33. R. K. Josephson, J. G. Malamud, D. R. Stokes, The efficiency of an asynchronous flight muscle from a beetle. *J. Exp. Biol.* **204**, 4125–4139 (2001).
 34. B. J. Borrell, M. J. Medeiros, Thermal stability and muscle efficiency in hovering orchid bees (Apidae: Euglossini). *J. Exp. Biol.* **207**, 2925–2933 (2004).
 35. C. Liu, P. Li, F. Song, E. J. Stamhuis, J. Sun, Design optimization and wind tunnel investigation of a flapping system based on the flapping wing trajectories of a beetle's hindwings. *Comput. Biol. Med.* **140**, 105085 (2022).
 36. C. P. Ellington, The aerodynamics of hovering insect flight. II. Morphological parameters. *Philos. Trans. R. Soc. Lond. B Biol. Sci.* **305**, 17–40 (1984).
 37. T. Weis Fogh, Quick estimates of flight fitness in hovering animals, including novel mechanisms for lift production. *J. Exp. Biol.* **59**, 169–230 (1973).
 38. F. T. Muijres, M. J. Elzinga, J. M. Melis, M. H. Dickinson, Flies evade looming targets by executing rapid visually directed banked turns. *Science* **344**, 172–177 (2014).
 39. Y. Liu, M. Sun, Wing kinematics measurement and aerodynamics of hovering droneflies. *J. Exp. Biol.* **211**, 2014–2025 (2008).
 40. P. Henningsson, R. J. Bomphrey, Time-varying span efficiency through the wingbeat of desert locusts. *J. R. Soc. Interface* **9**, 1177–1186 (2012).
 41. R. Dudley, Extraordinary flight performance of orchid bees (Apidae: Euglossini) hovering in heliox (80% He/20% O₂). *J. Exp. Biol.* **198**, 1065–1070 (1995).
 42. M. Keennon, K. Klingebiel, H. Won, A. Andriukov, Development of the nano hummingbird: A tailless flapping wing micro air vehicle, in *50th AIAA Aerospace Sciences Meeting Including the New Horizons Forum and Aerospace Exposition* (AIAA, 2012), p. 588.
 43. L. Hines, D. Campolo, M. Sitti, Liftoff of a motor-driven, flapping-wing microaerial vehicle capable of resonance. *IEEE Trans. Robot.* **30**, 220–232 (2014).
 44. X. Yang, Y. Chen, L. Chang, A. A. Calderon, N. O. Perez-Arancibia, Bee⁺: A 95-mg four-winged insect-scale flying robot driven by twinned unimorph actuators. *IEEE Robot. Autom. Lett.* **4**, 4270–4277 (2019).
 45. G. C. H. E. de Croon, M. A. Groen, C. de Wagter, B. Remes, R. Ruijsink, B. W. van Oudheusden, Design, aerodynamics and autonomy of the Delfly. *Bioinspir. Biomim.* **7**, 025003 (2012).
 46. Y. M. Chukewad, A. T. Singh, J. M. James, S. B. Fuller, A new robot fly design that is easier to fabricate and capable of flight and ground locomotion, in *IEEE International Conference on Intelligent Robots and Systems (IROS)* (IEEE, 2018), pp. 4875–4882.
 47. S. Deng, M. Percin, B. van Oudheusden, Experimental investigation of aerodynamics of flapping-wing micro-air-vehicle by force and flow-field measurements. *AIAA J.* **54**, 588–602 (2016).
 48. Y. Zou, W. Zhang, Z. Zhang, Liftoff of an electromagnetically driven insect-inspired flapping-wing robot. *IEEE Trans. Robot.* **32**, 1285–1289 (2016).
 49. M. Azhar, D. Campolo, G. K. Lau, L. Hines, M. Sitti, Flapping wings via direct-driving by DC motors, in *IEEE International Conference on Robotics and Automation (ICRA)* (IEEE 2013), pp. 1397–1402.
 50. I. Kroo, P. Kunz, Development of the Mesicopter: A miniature autonomous rotorcraft, in *Proceedings of American Helicopter Society Vertical Lift Aircraft Design Conference* (2000).
 51. T. Zadar, 2018 Cheerson CX-Stars Quadcopter Review; www.rcproreviews.com/cheerson-cx-stars-quadcopter/.
 52. J. T. Huber, J. S. Noyes, A new genus and species of fairyfly, *Tinkerbella nana* (Hymenoptera, Mymaridae), with comments on its sister genus *Kikiki*, and discussion on small size limits in arthropods. *J. Hymenopt. Res.* **32**, 17–44 (2013).
 53. Q. Boehler, S. Gervasoni, S. L. Charreyron, C. Chautems, B. J. Nelson, On the workspace of electromagnetic navigation systems. *IEEE Trans. Robot.* **39**, 791–807 (2022).
 54. S. Gervasoni, M. Pedrini, T. Rifai, C. Fischer, F. C. Landers, M. Mattmann, R. Dreyfus, S. Viviani, A. Veciana, E. Masina, B. Aktas, J. P. Luis, C. Chautems, S. Pane, Q. Boehler, P. Gruber, B. J. Nelson, A human-scale clinically ready electromagnetic navigation system for magnetically responsive biomaterials and medical devices. *Adv. Mater.* **36**, 2310701 (2024).
 55. R. Chen, D. Folio, A. Ferreira, Mathematical approach for the design configuration of magnetic system with multiple electromagnets. *Robot. Auton. Syst.* **135**, 103674 (2021).
 56. J. Illingworth, J. Kittler, A survey of the Hough transform. *Comput. Vis. Graph. Image Process.* **44**, 87–116 (1988).
 57. D. Ziou, S. Tabbone, Edge detection techniques—an overview. *Pattern Recognit. Image Anal.* **8**, 537–559 (1998).
 58. E. T. K. Chiang, T. Mashimo, Development of micro ultrasonic actuator and micro rotor blade for micro aerial vehicle, in *IEEE/RJSJ International Conference on Intelligent Robots and Systems (IROS)* (IEEE, 2019), pp. 6058–6063.
 59. C. T. David, The relationship between body angle and flight speed in free-flying *Drosophila*. *Physiol. Entomol.* **3**, 191–195 (1978).
- Acknowledgments:** We thank H. Taylor, D. Liepmann, K. Pister, V. Carey, Y. Wu, J. Liang, R. Xu, R. Guo, Y. Huang, B. Zhang, and D. Wang for the helpful discussions. We thank the Jacobs Institute for Design Innovation, UC Berkeley for providing the 3D printers. **Funding:** This work was supported by Berkeley Sensor and Actuator Center. **Author contributions:** Conceptualization: L.L., F.S., and W.Y. Methodology: F.S. Investigation: F.S., W.Y., Y.G., and K.B. Resources: L.L., F.S., and W.Y. Validation: F.S., W.Y., K.B., Y.G., and L.L. Visualization: W.Y., F.S., K.B., Y.G., and L.L. Supervision: L.L., M.M., and F.S. Data curation: F.S. and W.Y. Formal analysis: W.Y., F.S., K.B., and M.M. Software: W.Y. and F.S. Writing—original draft: F.S., W.Y., and L.L. Writing—review and editing: L.L., W.Y., F.S., Y.G., and M.M. Project administration: L.L. and F.S. Funding acquisition: L.L. **Competing interests:** The authors declare that they have no competing interests. **Data and materials availability:** All data needed to evaluate the conclusions in the paper are present in the paper and/or the Supplementary Materials.
- Submitted 26 August 2024
Accepted 25 February 2025
Published 28 March 2025
10.1126/sciadv.ads6858